RESEARCH ARTICLE
SPACE PHYSICS: MAGNETOSPHERIC PHYSICS

Earth and Planetary Physics
7: 100–108, 2023
doi: 10.26464/epp2023012

Modeling the energetic electron fluxes in the inner radiation belt based on a drift-source model

Zheng Xiang*, BinBin Ni*, YangXiZi Liu, XuDong Gu, Song Fu, Wei Xu, Xing Cao, Xin Ma, DeYu Guo, JunHu Dong, and JingLe Hu

Department of Space Physics, School of Electronic Information, Wuhan University, Wuhan 430072, China

Key Points:

- A drift-source model is used to simulate longitudinal distributions of quasi-trapped energetic electron fluxes produced by CRAND.
- The simulation results show that quasi-trapped energetic electron fluxes increase with longitudes before reaching the SAA regions.
- The distributions of trapped, quasi-trapped, and untrapped electrons along the orbit of Macau Science Satellite-1 are also simulated.

Citation: Xiang, Z., Ni, B. B., Liu, Y. X. Z., Gu, X. D., Fu, S., Xu, W., Cao, X., Ma, X., Guo, D. Y., Dong, J. H., and Hu, J. L. (2023). Modeling the energetic electron fluxes in the inner radiation belt based on a drift-source model. *Earth Planet. Phys.*, *7*(1), 100–108. http://doi.org/10.26464/epp2023012

Abstract: The Macau Science Satellite-1 (MSS-1), designed by the Macao University of Science and Technology and the National Space Science Center (NSSC) of China, is equipped to detect the fine structure of the magnetic field over the South Atlantic Anomaly (SAA) region, monitoring geomagnetic field variations, and obtaining the energetic electron spectrum distributions in the Earth's inner radiation belt. In this study, we simulate the distributions of trapped, quasi-trapped, and untrapped electrons along the orbit of MSS-1 based on a drift-source model. The simulation results show that the particle detector with 90° looking direction can observe trapped electrons in the SAA region, untrapped electrons in the regions conjugated with the SAA region at the north hemisphere, and quasi-trapped electrons in all other regions. In contrast, the detectors with <60° looking directions can measure only untrapped electrons. Generally, quasi-trapped electron fluxes accumulate along the drift trajectory and are due primarily to CRAND, until reaching the SAA region where quasi-trapped electrons are all lost into the atmosphere.

Keywords: Earth's inner belt; drift-source model; quasi-trapped electron; CRAND

---

1. Introduction

In 1958, James A. Van Allen and co-workers, using data from Geiger counters onboard the Explorer 1 and Explorer 3 satellites, discovered high radiation zones surrounding the Earth (Van Allen et al., 1958), the first major discovery of the Space Age. These regions, filled with energetic particles, were later called "radiation belts" or "Van Allen Belts". Since that time, many spacecrafts have been launched to investigate the variation characteristics and underlying physical mechanisms of the Van Allen belts (Johnson and Kierein, 1992; Baker et al., 1993, 2013a).

Typically, radiation belts are divided into the inner belt and the outer belt with a slot region lying between. The inner belt (centered near L = ~1.5, where L represents the geocentric distance of the magnetic field lines at the equatorial plane in the number of Earth radii (R_E)) contains electrons of energy less than one MeV and protons of higher energy (up to several hundreds of MeV). The outer radiation belt consists of electrons over a broad energy range, from 100s of keV to 10s of MeV (Williams, 1966; Barker et al., 2005; Li X et al., 2013; Li W and Hudson, 2019). Generally, the radiation belt electron fluxes increase rapidly during geomagnetically active times and experience slow decay during quiet periods (Baker et al., 2013b; Li X et al., 2013; Xiang Z et al., 2017, 2020a, 2021). The variations of radiation belt electrons are consequences of complex competition among various transport, acceleration, and loss processes (Reeves et al., 2003, 2016; Huang et al., 2018; Turner et al., 2019; Gu XD et al., 2020; Du et al., 2022; Zhao et al., 2022).

Satellites used to observe the radiation belts can be mainly classified into two categories: low-Earth orbit (LEO) (high inclination) and equatorial (low inclination) satellites (e.g., Baker et al., 1993, 2013b; Parrot, 2006; Li X et al., 2013; Mauk et al., 2013; Angelopoulos et al., 2020; Khoo et al., 2022). The particle detectors onboard low inclination satellites can obtain wide coverage of pitch angles (the angles between particle moving directions and the background magnetic field). However, orbit periods of those satellites are typically a few hours, making it difficult to investigate short-term radiation belt dynamics, such as electron dropouts in the outer belt (Ni BB et al., 2016; Xiang Z et al., 2017, 2018; Tu WC et al., 2019; Ma X et al., 2020). In contrast, the orbit periods of LEO satellites are around 100 minutes, which allow more frequent monitoring of

---

Correspondence to: Z. Xiang, xiangzheng@whu.edu.cn
B. B. Ni, bbni@whu.edu.cn
Received 05 OCT 2022; Accepted 25 OCT 2022.
Accepted article online 13 DEC 2022.

radiation belt particle distributions (Ni BB et al., 2022a; Selesnick et al., 2019; Li XQ et al., 2019). In addition, due to the small values of loss cone angle at the equatorial plane (e.g., only a few degrees in the outer radiation belt), only those satellites with extremely high pitch-angle resolution can resolve precipitation electrons, whereas the larger loss cone angle at the altitudes of LEO satellites allows for more accurate identification of precipitating and quasi-trapped populations. (Li XL et al., 2017; Xiang Z et al., 2019; Zhang K et al., 2017, 2019; Zhang ZX et al., 2022). Due to the off-center nature of the Earth's actual magnetic field, electrons in the radiation belt can be categorized into three types: untrapped electrons (equatorial pitch angle smaller than local bounce loss cone (BLC), that will precipitate in one bounce period), quasi-trapped electrons (equatorial pitch angle larger than local BLC but smaller than the drift loss cone (DLC), which is the largest local BLC across the electron full drift orbit, thus with life times longer than several bounce periods but shorter than one drift period), and trapped electrons (stably trapped by the Earth's magnetic field, with lifetimes longer than a drift period). One of the most important advantages of LEO satellites is that they can measure and distinguish these three types using a single particle detector.

Recently, particle observations from the LEO satellites have significantly advanced our understanding of inner belt dynamics, especially some surprising discoveries from CubeSat missions. For example, the inner belt electrons had long been considered to be replenished by inward radial diffusion, until Li XL et al. (2017), based on convincing evidence provided by data from the Colorado Student Space Weather Experiment CubeSat (CSSWE), found that the relativistic electrons in the inner edge of the inner belt (L < 1.14) are produced primarily by Cosmic Ray Albedo Neutron Decay (CRAND). CRAND describes the process by which highly energetic particles from the galaxy collide with Earth's upper-atmosphere molecules and produce albedo neutrons with a mean lifetime of around 15 minutes. An albedo neutron decays naturally into a proton, an electron, and an antineutrino (Selesnick, 2015).

Several studies, comparing simulation results with observations from the DEMETER satellite, have followed, further suggesting that the electrons produced by the CRAND process also play an important role as source of energetic electron populations in the inner belt and in the slot regions during the extended quiet periods (Xiang Z et al., 2019, 2020a, b; Zhang K et al., 2019, 2020).

To detect the fine structure of the geomagnetic field over the South Atlantic Anomaly (SAA) region and to obtain the energetic electron spectrum distribution in the inner radiation belt, the Macao University of Science and Technology and the National Space Science Center (NSSC) of China have designed and built the MSS-1, which is planned to be launched in 2023 into a low-Earth orbit (LEO) with an inclination of ~40° and an altitude of ~450 km. The main payloads onboard the MSS-1 are high precision fluxgate magnetometers and detectors of energetic particles. The advantages of the MSS-1's particle detectors are higher pitch angle resolution (with nine looking directions) and fine energy resolution (energy resolution ~10–20 keV at the burst mode). Particle detectors onboard LEO satellites have typically had a wide field of view (FOV, e.g., 40°–50°) with only one looking direction (Khoo et al., 2022). Because the electron fluxes at the LEO orbits are much lower than those at equatorial orbits, the wider FOV is needed to produce larger geometry factors. More looking directions will be particularly helpful to investigate radiation belt dynamics, especially in the study of precipitation electrons. Using the measurements from two perpendicular detectors onboard POES satellites, many studies have been conducted to analyze the spatio–temporal features and underlying physical mechanisms of particle losses (Turner et al., 2012; Ni BB et al., 2016, 2022b; Xiang Z et al., 2016). The ability to measure fluxes of 50–600 keV electrons from nine different looking directions, provided by detectors onboard the MSS-1 satellite, will make it possible to obtain simultaneous measurements of trapped, quasi-trapped, and untrapped electrons, which is of critical importance for quantifying the scattering process of electrons from larger pitch angles to the loss cones driven by wave–particle interactions or atmospheric collisions. Based on the improved resolution of electron fluxes that will be provided by the MSS-1's instruments, we can investigate the energy spectrum distribution, and sources and loss mechanisms of electrons over a wide energy range in the inner belt. In this paper, we simulate the spatial distribution of untrapped, quasi-trapped, and trapped electrons along the planned orbit (450 km altitude and 40° inclination) of the MSS-1 and the corresponding electron fluxes based on a drift-source model.

2. Orbit Coverage Simulation of the MSS-1

Based on the planned altitude (450 km) and inclination (40°), we first simulate the L and magnetic local time (MLT) coverage of the MSS-1. Using the IRBEM library, we simulated the L values at 450 km altitudes in the IGRF magnetic field model. Figure 1 displays the simulation results as a function of longitudes and latitudes. The light pink curve is a simulation orbit of MSS-1 in a drift period (~1.5 h). Due to the nondipole features of Earth's magnetic field, the L values at a given latitude are distinct at different longitudes. The L values can be as large as $L \approx 2.5$ close to south Australia and north America regions where, typically, L will be >1.5. It is interesting to note that there are no L < 1.1 regions in the [−100°, −40°] longitudes range corresponding to the SAA regions, (the center of which is denoted in Figure 1), because the altitudes for L < 1.1 in

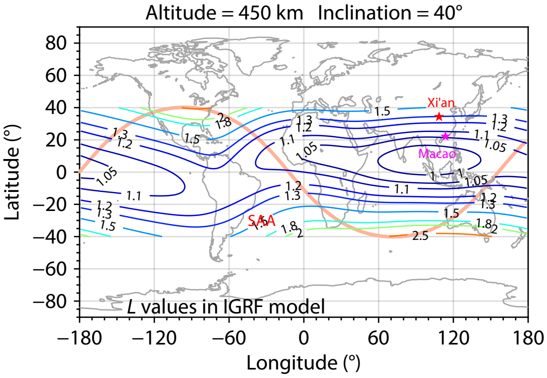

Figure 1. The L values at 450 km altitudes as a function of longitudes and latitudes. The light pink curve is a simulation orbit of MSS-1 in a drift period (~1.5 h).

these SAA regions are below the satellite's 450 km altitude.

In addition to *L* values, another important parameter of satellite orbit coverage is MLT. We simulate 10-hour satellite orbits with four different ascending nodes and plot them in Figure 2 on the MLT versus *L*-shell plane. The trajectories are color-coded by their universal times. In Figure 2, it is easy to observe that the maximum *L*-shell is at $L = \sim 2.5$. The local time coverage has strong ascending node dependence. In the simulation results, the satellite will sweep the nearly constant MLT range six times at low *L*-shell ($L < 2$) in the 10 hours. As time goes by, the local time of the satellite orbit will move clockwise. Typically, the electron fluxes along the drift shell are assumed independent of MLT since the drift period of energetic electrons is relatively low. However, observations from MagEIS instrument onboard Van Allen Probes clearly show that inner belt energetic electron fluxes at different MLT are distinct (Selesnick et al., 2016; Liu Y et al., 2016), with higher intensities near dawn sectors. This phenomenon can be explained by a global dawn-to-dusk convection electric field (Liu Y et al., 2016; Lejosne and Mozer, 2020). The fluctuations in the electric field result in inward diffusion, which replenishes electron losses induced by wave–particle interactions and atmospheric collisions. The gradually clockwise movement, as shown in Figure 2, can greatly help investigate the influence of convection electric field on energetic electron distributions.

3. Modeling the Distributions of Energetic Electrons in the Inner Belt

In this section, we first simulate the spatial distributions of the three types of electrons: untrapped, quasi-trapped, and trapped. We obtain magnetic field strengths using the IGRF model and assume that electrons precipitate into the atmosphere below 100 km altitudes. In the simulation, the looking directions (the angle between the detector collimator and the background magnetic field, the detector with the 90° looking direction is perpendicular to the background magnetic field and thus detects electrons with a 90° local pitch angle) of detectors are set as 90°, 80°, 70°, and 60°. In reality, the actual looking directions of detectors change with the satellite's changing position and attitude. For simplicity, in the simulations we set these looking direction values as constants. The incident direction of electrons is assumed to be perpendicular to the plane of the detector, although the field of view (FOV) of the detectors is around 20°–30°.

The simulation results are shown in Figure 3. We can observe that the 90° detector can measure trapped electrons in the SAA region, untrapped electrons in the conjugation regions of SAA at the north hemisphere, and quasi-trapped electrons in all other regions. As looking directions decrease, the area of untrapped electrons increases while the areas of trapped electrons and quasi-trapped electrons both shrink. In all regions, the <60° detectors measure only untrapped electrons.

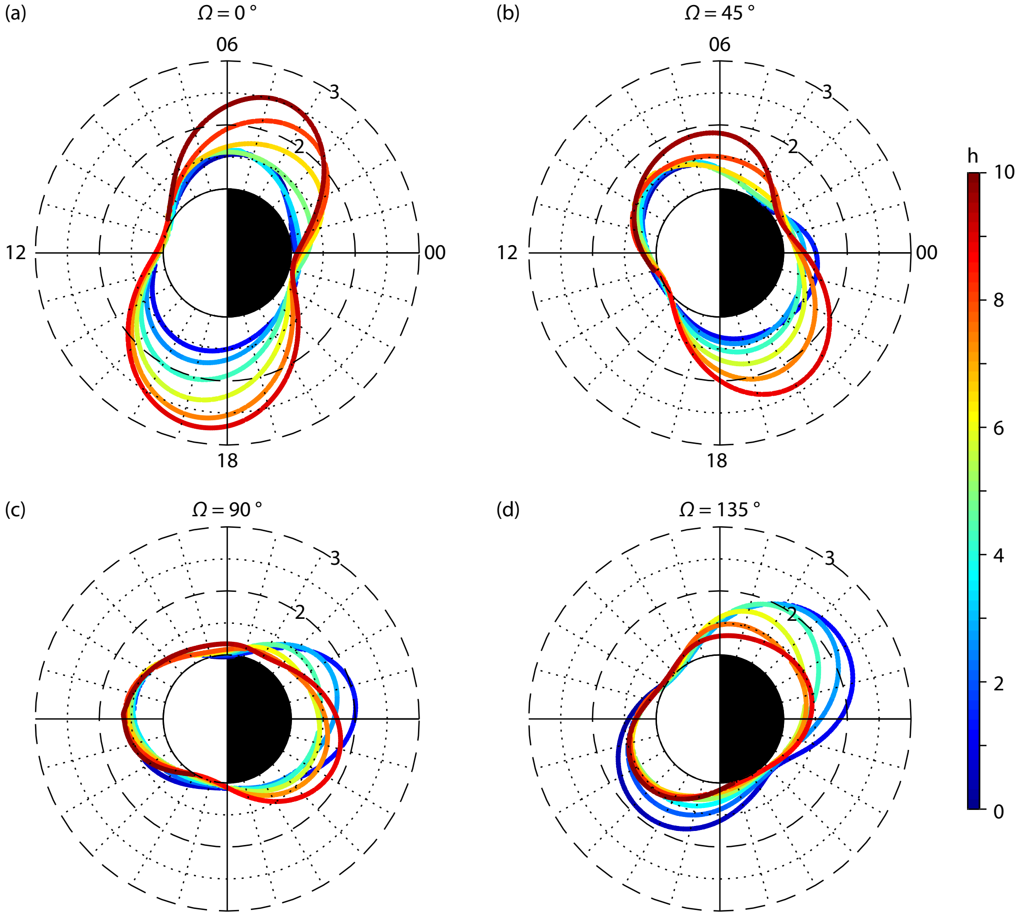

Figure 2. Simulated satellite trajectories in 10 hours as a function of MLT and *L*-shell, calculated with four ascending nodes: (a) 0°, (b) 45°, (c) 90°, and (d) 135°. The color indicates the universal time.

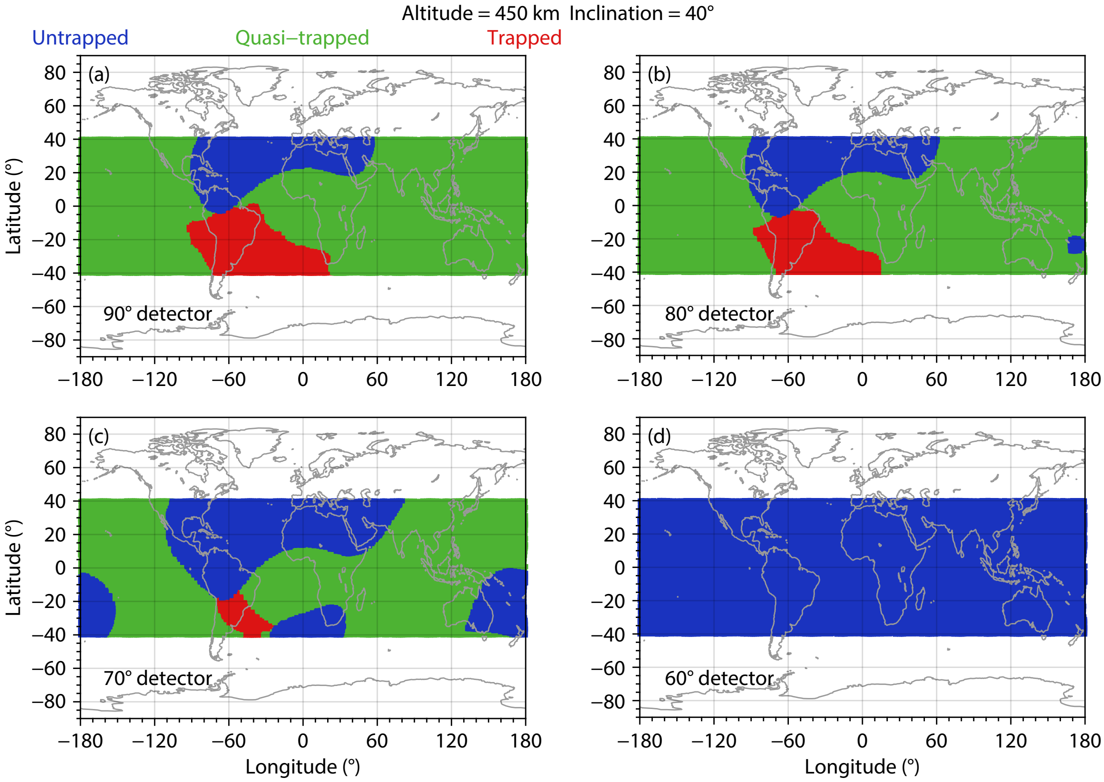

Figure 3. The simulation results of spatial distribution of trapped, quasi-trapped, and untrapped electrons for detectors with 90°, 80°, 70°, and 60° looking directions, based on an IGRF magnetic field model. The 90° detector is perpendicular to the background magnetic field; the local pitch angle of measured electrons is thus 90°. The untrapped, quasi-trapped, and trapped electrons are indicated in blue, green, and red, respectively.

To investigate the distribution of energetic electron fluxes in the inner belt, we use the drift-source model in Xiang Z et al. (2019) to simulate pitch angle distributions of electron fluxes along the electron drift shell. For a given L-shell and kinetic energy, the drift-source model is described by the equation:

$$\frac{\partial J}{\partial t} + \omega_{\mathrm{d}} \frac{\partial J}{\partial \phi} = S_{\mathrm{e}}, \tag{1}$$

where J is the electron flux, ω_{d} is the drift frequency, and ϕ is the geomagnetic longitude. S_{e} is the electron source rate from CRAND:

$$S_{\mathrm{e}} \cong \frac{q_0 \varphi(E)\, \upsilon}{L^{2.7} \sin(\alpha_{\mathrm{eq}})}, \tag{2}$$

where the unit of q_0 is cm^{-3} sec^{-1} ster^{-1} and varies with L-shell. In our simulation, we adopt the q_0 value used in Xiang Z et al. (2019), that is, 10^{-13} at $L = 1.08$, 2×10^{-13} at $L = 1.5$, and 5×10^{-13} at $L = 2.0$. α_{eq} is the equatorial pitch angle, and $\varphi(E)$ is the β-decay spectrum of the electrons produced by neutron decay (Selesnick, 2015). There are 900 grid points in equatorial pitch angles and 360 grid points in longitudes. The boundary condition is $J = 0$ at the edge of the BLC. The magnetic field strength at 100 km altitude and at the geomagnetic equator is used to calculate the corresponding equatorial pitch angles of electrons mirroring at 100 km (Xiang Z et al, 2019).

The drift-source model assumes that electrons in the inner belt are mainly controlled by azimuthal drift and CRAND (Zhang K et al., 2019; Xiang Z et al., 2019). The excellent agreement between drift-source model simulations and DEMETER observations suggests that CRAND is an important source mechanism for inner belt electrons (Xiang Z et al., 2019). After adding the diffusion term (e.g., pitch angle diffusion induced by wave–particle interactions) and an advection term (e.g., energy loss due to Coulomb drag), the drift-source model can also be used to investigate the dynamics and the evolution of trapped electron fluxes in the inner belt and the slot region (Xiang Z et al., 2020a, b; Liu YXZ et al., 2021; 2022).

We first run the simulations for $L = 1.08$, $L = 1.5$, and $L = 2.0$ in the drift-source model. The simulation results are shown in Figure 4. The left column presents color-coded simulated electron fluxes at 200 keV as a function of geomagnetic longitudes and equatorial pitch angles. The dashed black line is the local BLC calculated in the IGRF model, and the electron fluxes are set as zero in BLC, indicated by the blank parts. Note that the 180° east longitude is also the −180° west longitude at the horizon axis. In Figure 4a, the largest local BLC (the DLC) is 90°, occurring in the SAA region (longitude = ~−60°), indicating that the electrons at $L = 1.08$ are all quasi-trapped. The light pink and blue markers are the equatorial pitch angles of locally mirroring electrons at 450 km altitude (the planned orbit altitude of the MSS-1). The simulated electron fluxes corresponding to these markers are plotted as a function of geomagnetic longitudes, shown in the right panel (Figures 4b, 4d, 4e). We can see that electron fluxes in the simulations accumulate along the longitude before reaching the SAA region. At higher L-shell ($L = 1.5$), electrons with pitch angles larger than the DLC (39° at longitude = ~−50°) are trapped electrons; they will not precipi-

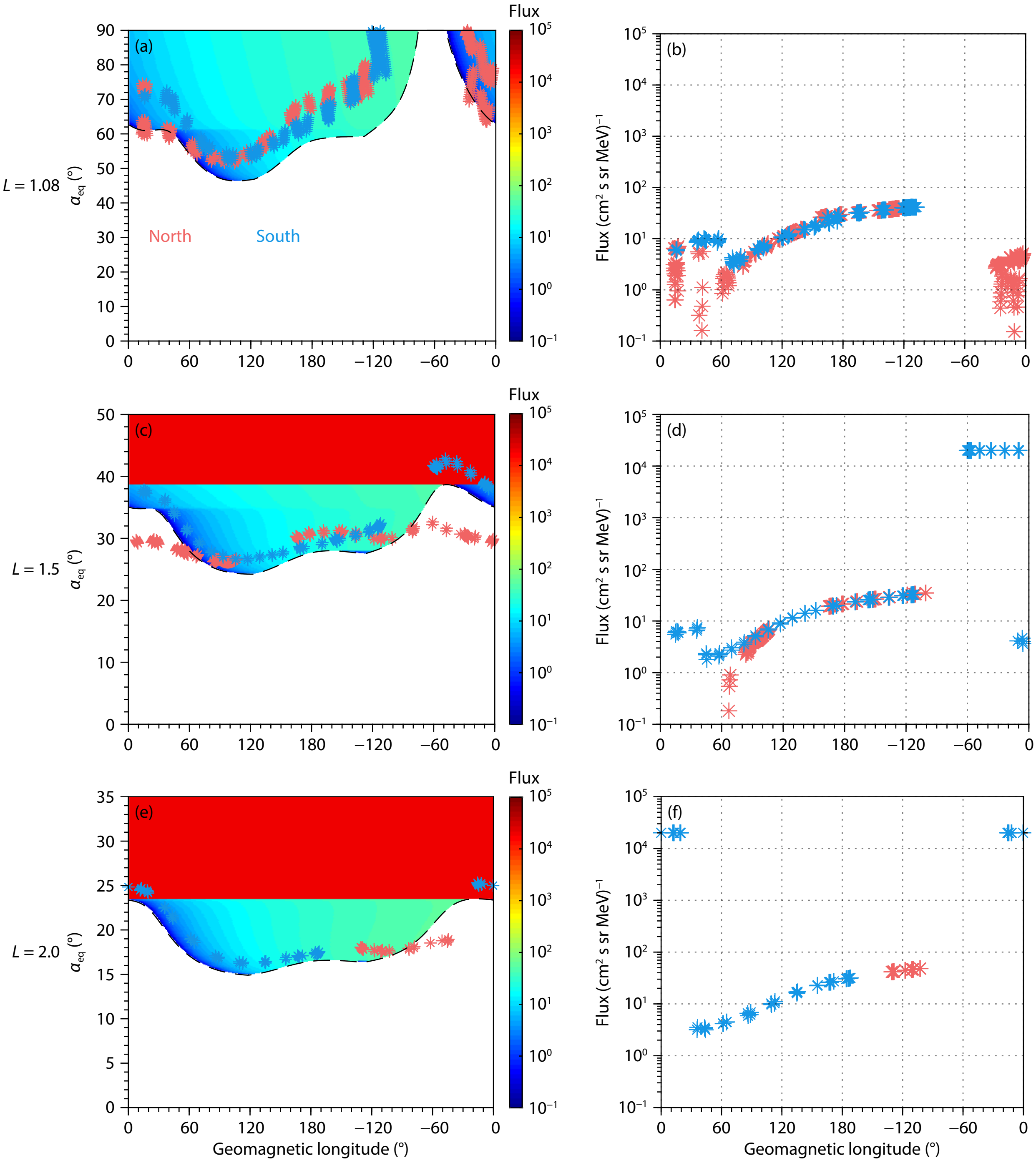

Figure 4. LEFT COLUMN: Simulated color-coded fluxes of 200 keV electrons, as a function of geomagnetic longitude and the equatorial pitch angle in one drift period at (from top to bottom) (a) L = 1.08, (c) L = 1.5, and (e) L = 2.0. The dashed black line is the local BLC calculated in the IGRF model, and the electron fluxes are set as zero in BLC, indicated by the blank parts. The light pink and blue markers are the equatorial pitch angles of local mirror electrons at 450 km altitude on the northern and southern hemispheres, respectively. RIGHT COLUMN: The longitudinal distributions of simulated electron fluxes, corresponding to the markers in the left panels. Note that the 180° east longitude is also the −180° west longitude.

tate (Figure 4c) during the drift. The longitudinal distribution features of quasi-trapped electrons are similar to results (Figure 4b) at different L values. Note that there are some data missing in some longitude ranges, such as ~−90° longitude in the southern hemisphere and ~130° longitude in the northern hemisphere, since some L values are not covered by the 450 km altitude at those longitudes. It can also be observed in Figure 1 that the contour curve of L = 1.5 is discontinuous at around −110° to −60° longitudes in the south hemisphere and 100°–160° longitudes in the north hemisphere. At L = 2 (Figure 4e and Figure 4f), longitudes for which data are missing become even broader. Electrons in the north hemisphere are measured only at around longitudes −130°

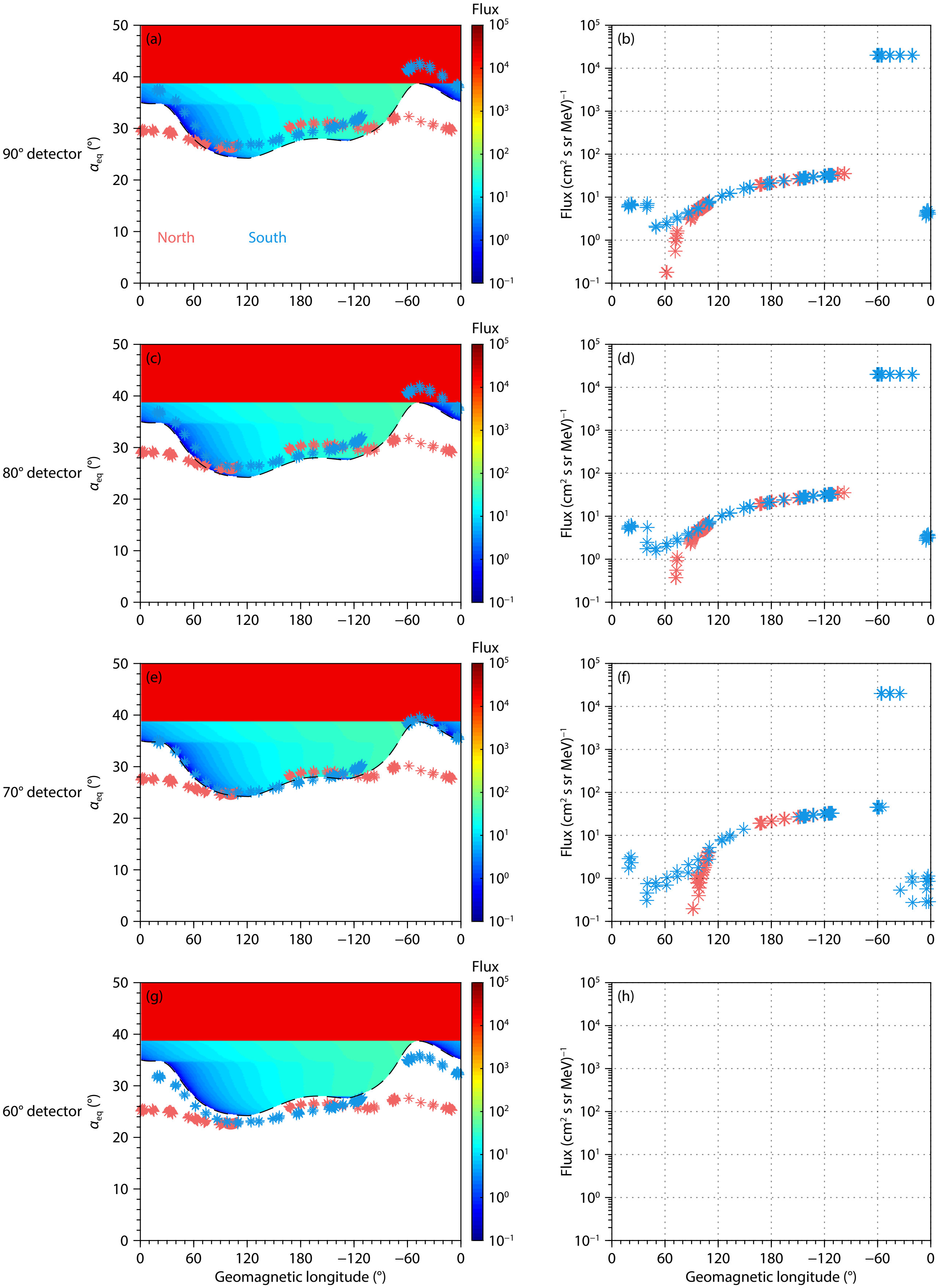

Figure 5. The simulation results of 200 keV electron fluxes measured by (from top to bottom) 90°, 80°, 70°, and 60° detectors at L = 1.5, in the same format as Figure 4. Note that the 180° east longitude is also the −180° west longitude.

to −30° while electrons in the south hemisphere can be measured at most longitudes except −130° to −30°.

To investigate electron flux variations with distinct looking directions of detectors, we simulated 200 keV electron fluxes at $L = 1.5$ measured by 90°, 80°, 70°, and 60° detectors; results are presented in Figure 5. The results in Figures 5a–5b (90° detectors) are the same as those in Figures 4c–4d. We can observe that the equatorial pitch angles of electrons shift to lower values as looking directions of detectors decrease. In Figure 5g, only untrapped electrons are measured in both north and south hemispheres, which is consistent with the results in Figure 3b. In the right panels, the longitudinal distribution characteristics of electrons measured by the 90°, 80°, and 70° detectors are similar since these quasi-trapped electrons are all from CRAND, which has slight pitch angle dependence outside of loss cones (Xiang Z et al., 2019).

In this study, we consider only the CRAND source and electron azimuthal drift without any loss mechanism. However, pitch angle diffusions induce by VLF transmitter signals can also play a role in the distribution of electron fluxes in the inner belt. Previous studies have reported that the quasi-trapped electron fluxes at 200 keV measured by the LEO satellite are sharply enhanced at around L = 1.6–1.8, corresponding to the location of the NWC transmitter (e.g. Sauvaud et al., 2008; Gamble et al., 2008; Selesnick et al., 2013; Zhang ZX et al., 2016; Zhang ZX et al., 2021). By adding the wave diffusion term induced by VLF signals into the drift-source model, the simulated quasi-trapped electron fluxes evidently enhance at longitude = 120° (where the NWC transmitter is located) and keep drifting eastward until lost into the SAA region. The agreement between the simulations and the DEMETER observations demonstrates that trapped electrons scattered by VLF transmitter signals are the dominant source of quasi-trapped electrons at $L = 1.7$ when the NWC transmitter operates at nightside (Liu YXZ et al., 2022), whereas, using the electron data of PROBA-V, Cunningham et al. (2020) found that there is a peak in the radial profile of electron fluxes in the [600,700] keV channel at $L = 1.5$, which satisfy the cyclotron resonance between electrons and unducted VLF transmitter signals. The fluxes of ~700 keV electrons measured by DEMETER are not accurate. Thus, the wave induced enhancement of ~700 keV electron fluxes needs to be further examined by other satellite observations.

4. Summary

In this study, we simulate L and MLT coverage of MSS-1 satellite (the planned orbit is at 450 km altitude and 40° inclination) and the distributions of electron populations (trapped, quasi-trapped, and untrapped) based on the IRBEM library and drift-source model.

The main simulation results are summarized as below:

(1) The orbits of the MSS-1 satellite will cover primarily the inner belt, with largest L values around $L = 2.5$; the orbits move clockwise, covering all MLT sectors.

(2) At 450 km altitude, detectors with the 90° looking direction will detect trapped electron in the SAA regions, untrapped electrons in the regions conjugate to SAA regions in the north hemisphere, and quasi-trapped electron in all other regions. The detectors with <60° looking directions will measure untrapped electrons.

(3) CRAND-produced electrons accumulate during drift trajectories outside the SAA regions. The fluxes of trapped electrons observed in the SAA regions are orders of magnitude higher than fluxes of quasi-trapped electrons.

Acknowledgments

This work was supported by the National Natural Science Foundation of China (Grant Nos. 42188101, 42174190, 42025404, 41904143, 41974186, and 41904144), the Fundamental Research Funds for the Central Universities (2042021kf0016), the B-type Strategic Priority Program of the Chinese Academy of Sciences (Grant No. XDB41000000), the pre-research projects on Civil Aerospace Technologies funded by the China National Space Administration (Grant Nos. D020303, D020308, D020104), and the China Postdoctoral Science Foundation Project (Grant No. 2019M662700, 2020M672405). The IRBEM library is available at https://prbem.github.io/IRBEM.

References

Angelopoulos, V., Tsai, E., Bingley, L., Shaffer, C., Turner, D. L., Runov, A., Li, W., Liu, J., Artemyev, A. V., ... Zhang, G. Y. (2020). The ELFIN Mission. *Space Sci. Rev.*, *216*(5), 103. https://doi.org/10.1007/s11214-020-00721-7

Baker, D. N., Mason, G. M., Figueroa, O., Colon, G., Watzin, J. G., and Aleman, R. M. (1993). An overview of the Solar Anomalous, and Magnetospheric Particle Explorer (SAMPEX) mission. *IEEE Trans. Geosci. Remote Sens.*, *31*(3), 531–541. https://doi.org/10.1109/36.225519

Baker, D. N., Kanekal, S. G., Hoxie, V. C., Batiste, S., Bolton, M., Li, X., Elkington, S. R., Monk, S., Reukauf, R., ... Friedel, R. (2013a). The Relativistic Electron-Proton Telescope (REPT) instrument on board the Radiation Belt Storm Probes (RBSP) spacecraft: Characterization of Earth's radiation belt high-energy particle populations. *Space Sci. Rev.*, *179*(1), 337–381. https://doi.org/10.1007/s11214-012-9950-9

Baker, D. N., Kanekal, S. G., Hoxie, V. C., Henderson, M. G., Li, X., Spence, H. E., Elkington, S. R., Friedel, R. H. W., Goldstein, J., ... Claudepierre, S. G. (2013b). A long-lived relativistic electron storage ring embedded in Earth's outer Van Allen belt. *Science*, *340*(6129), 186–190. https://doi.org/10.1126/science.1233518

Barker, A. B., Li, X., and Selesnick, R. S. (2005). Modeling the radiation belt electrons with radial diffusion driven by the solar wind. *Space Wea.*, *3*(10), S10003. https://doi.org/10.1029/2004SW000118

Cunningham, G. S., Botek, E., Pierrard, V., Cully, C., and Ripoll, J. F. (2020). Observation of high-energy electrons precipitated by NWC transmitter from PROBA-V low-Earth orbit satellite. *Geophys. Res. Lett.*, *47*(16), e2020GL089077. https://doi.org/10.1029/2020gl089077

Du, H. L., Cao, X., Ni, B. B., Fu, S., Ma, X., Yun, X. T., Long, M. Y., and Luo, Q. (2022). Distribution of O^+ and O^+_2 fluxes and their escape rates in the near-Mars magnetotail: A survey of MAVEN observations. *Earth Planet. Phys.*, *6*(6), 536–545. https://doi.org/10.26464/epp2023002

Gamble, R. J., Rodger, C. J., Clilverd, M. A., Sauvaud, J. A., Thomson, N. R., Stewart, S. L., McCormick, R. J., Parrot, M., and Berthelier, J. J. (2008). Radiation belt electron precipitation by man-made VLF transmissions. *J. Geophys. Res. Space Phys.*, *113*(A10), A10211. https://doi.org/10.1029/2008ja013369

Gu, X. D., Xia, S. J., Fu, S., Xiang, Z., Ni, B. B., Guo, J. G., and Cao, X. (2020). Dynamic responses of radiation belt electron fluxes to magnetic storms and their correlations with magnetospheric plasma wave activities. *Astrophy. J.*, *891*(2), 127. https://doi.org/10.3847/1538-4357/ab71fc

Huang, J., Gu, X. D., Ni, B. B., Luo, Q., Fu, S., Xiang, Z., and Zhang, W. X. 2018. Importance of electron distribution profiles to chorus wave driven evolution of Jovian radiation belt electrons. *Earth Planet. Phys.*, *2*(5), 371-383. https://doi.org/10.26464/epp2018035

Johnson, M. H., and Kierein, J. (1992). Combined release and radiation effects satellite (CRRES): spacecraft and mission. *J. Spacecraft Rockets*, *29*(4), 556–563. https://doi.org/10.2514/3.55641

Khoo, L. Y., Li, X., Selesnick, R. S., Schiller, Q., Zhang, K., Zhao, H., Hogan, B., Cantilina, J. T., Sims A., ... Kohnert, R. (2022). On the challenges of measuring energetic particles in the inner belt: A Geant4 simulation of an energetic particle detector instrument, REPTile-2. *J. Geophys. Res.: Space Phys.*, *127*(4), e2021JA030249. https://doi.org/10.1029/2021JA030249

Lejosne, S., and Mozer, F. S. (2020). Experimental determination of the conditions associated with “zebra stripe” pattern generation in the Earth's inner radiation belt and slot region. *J. Geophys. Res.: Space Phys.*, *125*(7), e2020JA027889. https://doi.org/10.1029/2020JA027889

Li, W., and Hudson, M. K. (2019). Earth's Van Allen radiation belts: From discovery to the Van Allen Probes era. *J. Geophys. Res.: Space Phys.*, *124*(11), 8319–8351. https://doi.org/10.1029/2018JA025940

Li, X., Schiller, Q., Blum, L., Califf, S., Zhao, H., Tu, W., Turner, D. L., Gerhardt, D., Palo, S., ... Spence, H. (2013). First results from CSSWE CubeSat: Characteristics of relativistic electrons in the near-Earth environment during the October 2012 magnetic storms. *J. Geophys. Res.: Space Phys.*, *118*(10), 6489–6499. https://doi.org/10.1002/2013JA019342

Li, X. L., Selesnick, R., Schiller, Q., Zhang, K., Zhao, H., Baker, D. N., and Temerin, M. A. (2017). Measurement of electrons from albedo neutron decay and neutron density in near-Earth space. *Nature*, *552*(7685), 382–385. https://doi.org/10.1038/nature24642

Li, X. Q., Xu, Y. B., An, Z. H., Liang, X. H., Wang, P., Zhao, X. Y., Wang, H. Y., Lu, H., Ma, Y. Q., ... Nan, Y. F. (2019). The high-energy particle package onboard CSES. *Radiat. Detect. Technol. Methods*, *3*(3), 22. https://doi.org/10.1007/s41605-019-0101-7

Liu, Y., Zong, Q. G., Zhou, X. Z., Foster, J. C., and Rankin, R. (2016). Structure and evolution of electron “zebra stripes” in the inner radiation belt. *J. Geophys. Res.: Space Phys.*, *121*(5), 4145–4157. https://doi.org/10.1002/2015JA022077

Liu, Y. X. Z., Xiang, Z., Guo, J. G., Gu, X. D., Fu, S., Zhou, R. X., Hua, M., Zhu, Q., Yi, J., and Ni, B. B. (2021). Scattering effect of very low frequency transmitter signals on energetic electrons in Earth’s inner belt and slot region. *Acta Phys. Sin.* (*in Chinese*), *70*(14), 149401. https://doi.org/10.7498/aps.70.20202029

Liu, Y. X. Z., Xiang, Z., Ni, B. B., Li, X. L., Zhang, K., Fu, S., Gu, X. D., Liu, J., and Cao, X. (2022). Quasi-trapped electron fluxes induced by NWC transmitter and CRAND: Observations and simulations. *Geophys. Res. Lett.*, *49*(5), e2021GL097443. https://doi.org/10.1029/2021GL097443

Ma, X., Xiang, Z., Ni, B. B., Fu, S., Cao, X., Hua, M., Guo, D. Y., Guo, Y. J., Gu, X. D., ... Zhu, Q. (2020). On the loss mechanisms of radiation belt electron dropouts during the 12 September 2014 geomagnetic storm. *Earth Planet. Phys.*, *4*(6), 598–610. https://doi.org/10.26464/epp2020060

Mauk, B. H., Fox, N. J., Kanekal, S. G., Kessel, R. L., Sibeck, D. G., and Ukhorskiy, A. (2013). Science objectives and rationale for the Radiation Belt Storm Probes mission. *Space Sci. Rev.*, *179*(1-4), 3–27. https://doi.org/10.1007/s11214-012-9908-y

Ni, B. B., Xiang, Z., Gu, X. D., Shprits, Y. Y., Zhou, C., Zhao, Z., Zhao, Z. Y., Zhang, X. G., and Zuo, P. B. (2016). Dynamic responses of the Earth's radiation belts during periods of solar wind dynamic pressure pulse based on normalized superposed epoch analysis. *J. Geophys. Res.: Space Phys.*, *121*(9), 8523–8536. https://doi.org/10.1002/2016JA023067

Ni, B. B., Hua, M., Gu, X. D., Fu, S., Xiang, Z., Cao, X., and Ma, X. (2022a). Artificial modification of Earth’s radiation belts by ground-based very-low-frequency (VLF) transmitters. *Sci. China Earth Sci.*, *65*(3), 391–413. https://doi.org/10.1007/s11430-021-9850-7

Ni, B. B., Zhang, Y., and Gu, X. D. (2022b). Identification of ring current proton precipitation driven by scattering of electromagnetic ion cyclotron waves. *Fundamental Res.* https://doi.org/10.1016/j.fmre.2021.12.018

Parrot, M. (2006). Special issue of planetary and space science ‘DEMETER’. *Planet. Space Sci.*, *54*(5), 411–412. https://doi.org/10.1016/j.pss.2005.10.012

Reeves, G. D., McAdams, K. L., Friedel, R. H. W., and O'Brien, T. P. (2003). Acceleration and loss of relativistic electrons during geomagnetic storms. *Geophys. Res. Lett.*, *30*(10), 1529. https://doi.org/10.1029/2002GL016513

Reeves, G. D., Friedel, R. H. W., Larsen, B. A., Skoug, R. M., Funsten, H. O., Claudepierre, S. G., Fennell J. F., Turner D. L., Denton M. H., ... Baker, D. N. (2016). Energy-dependent dynamics of keV to MeV electrons in the inner zone, outer zone, and slot regions. *J. Geophys. Res.: Space Phys.*, *121*(1), 397–412. https://doi.org/10.1002/2015JA021569

Sauvaud, J. A., Maggiolo, R., Jacquey, C., Parrot, M., Berthelier, J. J., Gamble, R. J., and Rodger, C. J. (2008). Radiation belt electron precipitation due to VLF transmitters: Satellite observations. *Geophys. Res. Lett.*, *35*(9), L09101. https://doi.org/10.1029/2008GL033194

Selesnick, R. S., Albert, J. M., and Starks, M. J. (2013). Influence of a ground-based VLF radio transmitter on the inner electron radiation belt. *J. Geophys. Res.: Space Phys.*, *118*(2), 628–635. https://doi.org/10.1002/jgra.50095

Selesnick, R. S. (2015). High-energy radiation belt electrons from CRAND. *J. Geophys. Res.: Space Phys.*, *120*(4), 2912–2917. https://doi.org/10.1002/2014ja020963

Selesnick, R. S., Su, Y. J., and Blake, J. B. (2016). Control of the innermost electron radiation belt by large-scale electric fields. *J. Geophys. Res.: Space Phys.*, *121*(9), 8417–8427. https://doi.org/10.1002/2016JA022973

Selesnick, R. S., Su, Y. J., and Sauvaud, J. A. (2019). Energetic electrons below the inner radiation belt. *J. Geophys. Res.: Space Phys.*, *124*(7), 5421–5440. https://doi.org/10.1029/2019JA026718

Tu, W. C., Xiang, Z., and Morley, S. K. (2019). Modeling the magnetopause shadowing loss during the June 2015 dropout event. *Geophys. Res. Lett.*, *46*(16), 9388–9396. https://doi.org/10.1029/2019GL084419

Turner, D. L., Shprits, Y., Hartinger, M., and Angelopoulos, V. (2012). Explaining sudden losses of outer radiation belt electrons during geomagnetic storms. *Nat. Phys.*, *8*(3), 208–212. https://doi.org/10.1038/nphys2185

Turner, D. L., Kilpua, E. K. J., Hietala, H., Claudepierre, S. G., O'Brien, T. P., Fennell, J. F., Blake, J. B., Jaynes, A. N., Kanekal, S., ... Reeves, G. D. (2019). The response of Earth's electron radiation belts to geomagnetic storms: Statistics from the Van Allen Probes era including effects from different storm drivers. *J. Geophys. Res.: Space Phys.*, *124*(2), 1013–1034. https://doi.org/10.1029/2018JA026066

Van Allen, J. A., Ludwig, G. H., Ray, E. C., and McIlwain, C. E. (1958). Observation of high intensity radiation by satellites 1958 Alpha and Gamma. *J. Jet Propul.*, *28*(9), 588–592. https://doi.org/10.2514/8.7396

Williams, D. J. (1966). A 27-day periodicity in outer zone trapped electron intensities. *J. Geophys. Res.*, *71*(7), 1815–1826. https://doi.org/10.1029/JZ071i007p01815

Xiang, Z., Ni, B. B., Zhou, C., Zou, Z. Y., Gu, X. D., Zhao, Z. Y., Zhang, X. G., Zhang, X. X., Zhang, S. Y., ... Reeves, G. (2016). Multi-satellite simultaneous observations of magnetopause and atmospheric losses of radiation belt electrons during an intense solar wind dynamic pressure pulse. *Ann. Geophys.*, *34*(5), 493–509. https://doi.org/10.5194/angeo-34-493-2016

Xiang, Z., Tu, W. C., Li, X. L., Ni, B. B., Morley, S. K., and Baker, D. N. (2017). Understanding the mechanisms of radiation belt dropouts observed by Van Allen Probes. *J. Geophys. Res.: Space Phys.*, *122*(10), 9858–9879. https://doi.org/10.1002/2017JA024487

Xiang, Z., Tu, W. C., Ni, B. B., Henderson, M. G., and Cao, X. (2018). A statistical survey of radiation belt dropouts observed by Van Allen Probes. *Geophys. Res. Lett.*, *45*(16), 8035–8043. https://doi.org/10.1029/2018GL078907

Xiang, Z., Li, X. L., Selesnick, R., Temerin, M. A., Ni, B. B., Zhao, H., Zhang, K., and Khoo, L. Y. (2019). Modeling the quasi-trapped electron fluxes from cosmic ray albedo neutron decay (CRAND). *Geophys. Res. Lett.*, *46*(4), 1919–1928. https://doi.org/10.1029/2018GL081730

Xiang, Z., Li, X. L., Temerin, M. A., Ni, B. B., Zhao, H., Zhang, K., and Khoo, L. Y. (2020a). On energetic electron dynamics during geomagnetic quiet times in Earth's inner radiation belt due to atmospheric collisional loss and CRAND as a Source. *J. Geophys. Res.: Space Phys.*, *125*(2), e2019JA027678. https://doi.org/10.1029/2019JA027678

Xiang, Z., Li, X. L., Ni, B. B., Temerin, M. A., Zhao, H., Zhang, K., and Khoo L. Y. (2020b). Dynamics of energetic electrons in the slot region during geomagnetically quiet times: Losses due to wave-particle interactions versus a source from cosmic ray albedo neutron decay (CRAND). *J. Geophys. Res.: Space Phys.*, *125*(9), e2020JA028042. https://doi.org/10.1029/2020ja028042

Xiang, Z., Li, X. L., Kapali, S., Gannon, J., Ni, B. B., Zhao, H., Zhang, K., and Khoo, L. Y. (2021). Modeling the dynamics of radiation belt electrons with source and loss driven by the solar wind. *J. Geophys. Res.: Space Phys.*, *126*(6), e2020JA028988. https://doi.org/10.1029/2020JA028988

Zhang, K., Li, X., Schiller, Q., Gerhardt, D., Zhao, H., and Millan, R. (2017). Detailed characteristics of radiation belt electrons revealed by CSSWE/REPTile measurements: Geomagnetic activity response and precipitation observation. *J. Geophys. Res.*: *Space Phys.*, *122*(8), 8434–8445. https://doi.org/10.1002/2017ja024309

Zhang, K., Li, X., Zhao, H., Schiller, Q., Khoo, L. Y., Xiang, Z., Selesnick, R., Temerin, M. A., and Sauvaud, J. A. (2019). Cosmic Ray Albedo Neutron Decay (CRAND) as a source of inner belt electrons: Energy spectrum study. *Geophys. Res. Lett.*, *46*(2), 544–552. https://doi.org/10.1029/2018gl080887

Zhang, K., Li, X. L., Xiang, Z., Khoo, L. Y., Zhao, H., Looper, M. D., Temerin, M. A., and Sauvaud, J. A. (2020). Long-term variations of quasi-trapped and trapped electrons in the inner radiation belt observed by DEMETER and SAMPEX. *J. Geophys. Res.*: *Space Phys.*, *125*(9), e2020JA028086. https://doi.org/10.1029/2020JA028086

Zhang, Z. X., Li, X. Q., Wang, C. Y., and Chen, L. J. (2016). North west cape-induced electron precipitation and theoretical simulation. *Chin. Phys. B*, *25*(11), 119401. https://doi.org/10.1088/1674-1056/25/11/119401

Zhang, Z. X., Xiang, Z., Wang, Y. F., Ni, B. B., and Li, X. Q. (2021). Electron acceleration by magnetosonic waves in the deep inner belt (L = 1.5-2) region during geomagnetic storm of August 2018. *J. Geophys. Res.*: *Space Phys.*, *126*(12), e2021JA029797. https://doi.org/10.1029/2021JA029797

Zhang, Z. X., Li, X. Q., Wang, L., Zhima, Z., Shen, X. H., Yuan, S. G., An, Z. H., Xu, Y. B., Liang, X. H., ... Wen, X. Y. (2022). Evaluation of the proton contamination to MeV electrons by solar proton events based on CSES observations. *J. Geophys. Res.*: *Space Phys.*, *127*(9), e2022JA030550. https://doi.org/10.1029/2022JA030550

Zhao, Y. W., Xiang, Z., Gu, X. D., Ni, B. B., Ma, X., Lou, Y. Q., Jiao, L. H., Zhou, R. X., Guo, D. Y., Liu, Y. X. Z., and Dong, J. H. (2022). Simultaneous occurrence of four magnetospheric wave modes and the resultant combined scattering effect on radiation belt electrons. *Earth Planet. Phys.*, *6*(6), 563–575. https://doi.org/10.26464/epp2022050